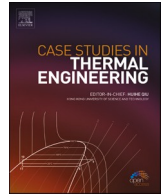




ELSEVIER

Contents lists available at [ScienceDirect](https://www.sciencedirect.com)

## Case Studies in Thermal Engineering

journal homepage: [www.elsevier.com/locate/csite](http://www.elsevier.com/locate/csite)

# Global domain fluid-thermal coupling modeling method and characteristics analysis for large capacity motor

Yongming Xu<sup>a,\*</sup>, Ziyi Xu<sup>b</sup>, Qianwen Zhao<sup>b</sup>, Yaodong Wang<sup>c</sup>

<sup>a</sup> School of Electrical and Information Engineering, Changzhou Institute of Technology, Changzhou, 213032, China

<sup>b</sup> School of Electrical and Electronic Engineering, Harbin University of Science and Technology, Harbin, 150080, China

<sup>c</sup> Department of Engineering, Durham University, Durham, DH1 3LE, UK

## ARTICLE INFO

Handling Editor: Huihe Qiu

### Index Terms:

—Large capacity electric machine  
Global domain fluid-thermal coupling model  
Modeling method  
Fluid-thermal characteristics

## ABSTRACT

—The global domain fluid-thermal characteristics study is challenging to perform due to the complicated ventilation arrangement and enormous volume for the large capacity electric machine. This paper uses the world's largest capacity non-superconducting low-speed induction motor, 6.5 MW, as the research object and proposes a global domain fluid-thermal characteristics calculation method. Firstly, the global domain fluid field model of the inner air path is established and solved. Then, the motor is divided into five subdomains according to the ventilation structure. The flow and pressure obtained from fluid field solutions are used as coupling parameters to couple each subdomain model, and an iterative solution is carried out based on the boundary condition continuity of the adjacent subdomains. The temperature distribution of each subdomain is obtained when the temperature difference is less than 0.1%. Finally, an experimental platform is built to verify the results. The maximum relative error between calculated and measured values is 1.67% for temperature and 4.92% for fluid velocity, which verifies the developed model's rationality and the proposed method's validity.

## 1. Introduction

Positive-pressure explosion-proof induction motors are frequently employed in flammable and explosive industrial production because of their superior explosion-proof performance [1]. When motor capacity and electromagnetic load grow, heat production per unit volume increases substantially, raising motor temperature and decreasing dependability. Hence, precise motor temperature prediction is crucial for steady operation of positive-pressure explosion-proof induction motors. Currently, fluid flow and heat transmission in positive-pressure explosion-proof induction motors and motor temperature prediction are hot research topics.

The current mainstream motor temperature prediction methods are the lumped parameter thermal network (LPTN) and the numerical analysis method [2]. LPTN can quickly calculate the motor temperature but relies on empirical formulas and coefficients [3,4]. Moreover, it cannot predict the fluid flow characteristics in the motor. In contrast, the numerical analysis method predicts motor temperature and fluid distribution accurately in complicated ventilation structures.

Stebel et al. [5] predicted the temperature distribution of the transformer by numerical analysis. And the effects of the cooling medium and ambient temperature on the temperature distribution and oil flow characteristics are revealed. Tiwari et al. [6] used the developed air-gap annulus model to perform a coupled calculation of the stator-rotor conjugate heat transfer model and determine the

\* Corresponding author.

E-mail address: [xuyongming@czu.cn](mailto:xuyongming@czu.cn) (Y. Xu).

<https://doi.org/10.1016/j.csite.2023.102860>

Received 28 December 2022; Received in revised form 22 February 2023; Accepted 24 February 2023

Available online 26 February 2023

2214-157X/© 2023 The Authors. Published by Elsevier Ltd. This is an open access article under the CC BY-NC-ND license (<http://creativecommons.org/licenses/by-nc-nd/4.0/>).

temperature distribution of the stator and rotor. Dang et al. [7] established a local conjugate heat transfer model for a hydrogenerator and investigated how the turbulence model affected calculation accuracy. Nategh et al. [8] developed thermal network models for both ends of the air-cooled traction motor and a 3D finite element model for the middle part. The finite element and thermal network models used fluid field data as thermal boundary conditions to determine temperature distribution under varied operating situations. Acquaviva et al. [9] reduced the three-dimensional numerical study by reducing the water jacket to a one-dimensional model, substituting the stator insulation and slot liner with thin walls, and utilizing convective heat transfer coefficients comparable for air gap and end winding heat transfer. Sung et al. [10] employed a dual-unit heat exchanger model to equal the motor's shell-and-tube heat exchanger model and examined the influence of folded tubes on motor cooling. Hosain and Kim et al. [11,12] used computational fluid dynamics (CFD) to investigate fluid flow and heat transfer in the air-gap during rotation. Tikadar et al. [13] numerically simulated the motor temperature and electromagnetic performance using stator sheath cooling, stator integrated cooling, and direct winding cooling. Bersch et al. [14] developed a 3D parametric conjugate heat transfer model for an air-cooled synchronous generator and coupled it with a 2D finite element electromagnetic model to predict the motor temperature. Appadurai et al. [15] studied the effect of the housing fin number and height on the temperature distribution. The results showed that the highest heat dissipation efficiency was achieved when 44 fins of 15 mm height were used. Sasa et al. [16] predicted flow rate and temperature distribution within a 10 MW superconducting generator using magneto-thermal coupling analysis. Kim et al. [17] predicted the MW class HTS synchronous motor temperature distribution using numerical analysis. By enhancing the thermal conductivity of the armature winding support, they improved hollow stator cooling. Carounagarane et al. [18] created a 3D numerical analytical model for a 250 MW hydrogenerator to anticipate temperature distribution under different overload conditions. Cotas et al. [19] used numerical simulation to analyze the effect of transient loads on transformer oil flow distribution and heat transfer. Kim et al. [20] studied the effect of the fan position of an oil-cooled transformer radiator on its cooling performance. Rodriguez et al. [21] numerically analyzed the radiator of a power transformer and obtained the heat dissipation, surface air velocity, and oil flow characteristics. Galloni et al. [22] used numerical analysis to determine how geometric features of motor cooling radial fans affect cooling capacity. All of the above literature investigated the flow-thermal characteristics of the motor through numerical simulation. However, they use local models or fast algorithms to reduce the solution time, resulting in lower computational accuracy. And for large motors with complex ventilation structures, the results obtained from the local model are difficult to accurately reflect the physical characteristics inside the motor.

The motor studied in this paper is the world's largest capacity non-superconducting low-speed induction motor. The cooling form is air-air cooled, and the cooler is located on top. The cooling airflow path comprises two independent air paths: inner and outer. The centrifugal fan at the center of the cooler's top drives the inner air path, while the axial fan at the outer air path's inlet drives it. This cooling system achieves a more uniform airflow distribution and less difference in temperature between the driven and non-driven ends. However, there is little literature on the fluid-thermal characteristics of the motor with this cooling method.

In light of those mentioned above, this paper establishes a 3D global domain fluid field model of the inner air path and a fluid-thermal characteristic analysis model of the core, ends, and cooler. And the method of coupling the fluid field model and the fluid-thermal characteristic analysis model is proposed. The flow law of the cooling medium inside the motor, global domain heat transfer properties, and motor temperature distribution are evaluated using the established model and proposed method. Finally, the rationality of the established model and the validity of the proposed method are verified through experiments. The proposed method can provide a reference for the analysis of the global domain fluid-thermal characteristics of large capacity motors.

## 2. Methodology

### 2.1. Prototype parameters and ventilation structure

The subject of this paper is a 6.5 MW positive-pressure explosion-proof air-air cooled induction motor, which is the world's largest non-superconducting low-speed induction motor. The performance parameters and basic dimensions are listed in Table 1.

The motor mainly consists of the stator core, stator winding, rotor core, rotor bar, shaft, rotor support frame, positive pressure housing, and cooler. The stator and rotor cores feature 14 equal-width and uniformly distributed radial ventilation ducts labeled No. 1 to No. 14 in order from left to right. The motor's cooling system is air-air cooled, and the cooler is positioned on top of the motor. The ventilated path is separated into inner and outer air paths, which are independent of one another, as shown in Fig. 1. The red arrow indicates the airflow direction in the inner air path. The inner air path is driven by the centrifugal fan positioned at the middle of the cooler's top, and the outer air path is driven by the axial fan located at the inlet of the outer air path. The cold air flowing from the

**Table 1**  
Performance parameters and basic dimensions of the prototype.

Item	Value	Item	Value
Rated power (MW)	6.5	Rated voltage (kV)	11
Rated speed (rpm)	297	Pole numbers	20
Stator outer diameter (mm)	2600	Number of stator slots	180
Stator inner diameter (mm)	2200	Number of rotor slots	210
Rotor outer diameter (mm)	2192	Cooling tube specifications	Φ23mm × 1.5 mm
Insulation class	F	Number of cooling tubes in the cooler	390
Outer diameter of the centrifugal fan (mm)	930	Inner diameter of the centrifugal fan (mm)	620
Outlet angle of the centrifugal fan blade (°)	49	Length of the centrifugal fan blade (mm)	186
Centrifugal fan blade numbers	16	Rated speed of the centrifugal fan (rpm)	1490

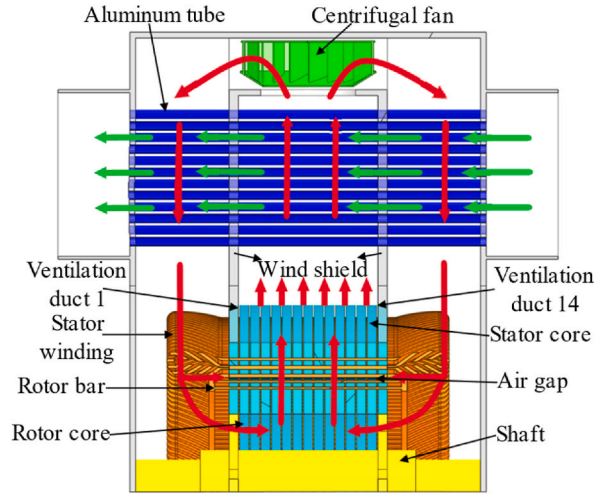


Fig. 1. Ventilated path of the prototype.

cooler first comes into contact with the end windings. Then, it flows axially through the rotor support frame and air gap. Lastly, the centrifugal fan at the top draws hot air from the core region down the radial ventilation ducts to the cooler, creating a circulation in the inner air path. The green arrow represents the direction of airflow in the outer air path. The cold air from outside enters the cooling tube and exchanges heat with the heated air in the inner air path through the tube wall to eliminate heat from the motor.

2.2. Mathematical model

Based on the theory of computational fluid dynamics and heat transfer, a mathematical model of fluid-thermal characteristic analysis is established, comprising mass conservation, momentum conservation, and energy conservation equations [23,24]:

$$\begin{cases} \frac{\partial(\rho u_i)}{\partial x_i} = 0 \\ \frac{\partial}{\partial x_i} (\rho u_i u_j) = -\frac{\partial p}{\partial x_i} + \frac{\partial}{\partial x_j} \left[ (\mu + \mu_t) \frac{\partial u_i}{\partial x_j} \right] \\ \frac{\partial}{\partial x_i} (u_i \rho c_p T) = \frac{\partial}{\partial x_j} \left( k_{eff} \frac{\partial T}{\partial x_j} + u_i (\tau_{ij})_{eff} \right) \end{cases} \quad (1)$$

where  $\rho$  is the density ( $\text{kg}/\text{m}^3$ ),  $k_{eff}$  is the thermal conductivity [ $\text{W}/(\text{m}\cdot\text{K})$ ],  $c_p$  is the specific heat [ $\text{J}/(\text{kg}\cdot^\circ\text{C})$ ] and  $T$  is the temperature ( $^\circ\text{C}$ ).

The Reynolds number of the fluid in the air gap and radial ventilation ducts is greater than 2300 and in a turbulent state. The shear stress transport (SST)  $k-\omega$  model is applied to solve complex turbulent motions in the fluid region, and the turbulence model control equation is as follows [25]:

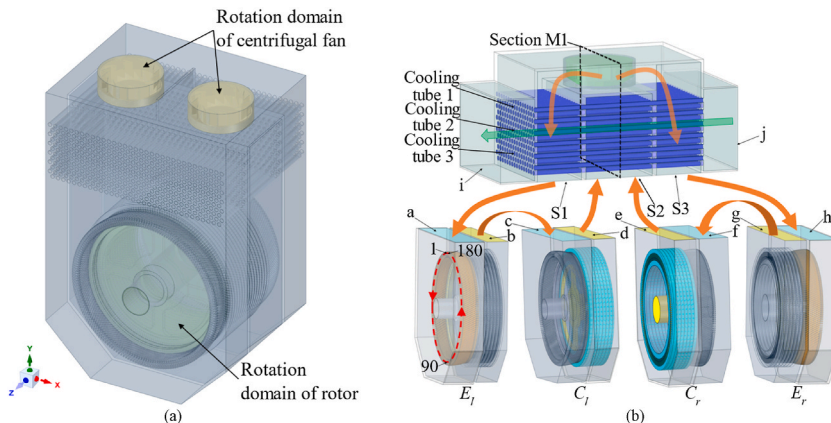


Fig. 2. 3D model. (a) 3D global domain fluid characteristic analysis model of the inner air path. (b) Fluid-thermal characteristics analysis model.

$$\begin{cases} \frac{\partial}{\partial x_j}(\rho k u_i) = \frac{\partial}{\partial x_j} \left[ \left( \mu + \frac{\mu_t}{\sigma_k} \right) \frac{\partial k}{\partial x_j} \right] + G_k - Y_k \\ \frac{\partial}{\partial x_j}(\rho \omega u_j) = \frac{\partial}{\partial x_j} \left[ \left( \mu + \frac{\mu_t}{\sigma_\omega} \right) \frac{\partial \omega}{\partial x_j} \right] + G_\omega - Y_\omega + D_\omega \end{cases} \quad (2)$$

where  $\sigma_k$  and  $\sigma_\omega$  are the turbulent Prandtl numbers for  $k$  and  $\omega$ ,  $G$  and  $Y$  represent the production of turbulence kinetic energy and the dissipation of  $k$  and  $\omega$ , respectively.

### 2.3. 3D global domain fluid field model

The 3D global domain fluid field model of the inner air path of the prototype is shown in Fig. 2(a). The model is built according to the actual dimensions and cooling arrangement of the motor. The solution domain includes the rotating fluid domain of the centrifugal fan and the rotor support frame and other non-rotating fluid domains.

According to the requirements of engineering calculations, the following assumptions and boundaries are made:

- 1) The air flow inside the motor is constant flow.
- 2) The effect of gravity on air flow is ignored.
- 3) The air velocity is much lower than the speed of sound, so it is considered to be an incompressible fluid.
- 4) The rotor rotates counterclockwise at 297 rpm when viewed from the positive direction of the Z-axis, and the centrifugal fan rotates clockwise at 1490 rpm when viewed from the positive direction of the Y-axis.

### 2.4. Fluid-thermal characteristic analysis model

Due to the complex ventilation structure and large size, it is difficult to conduct the global domain fluid-thermal characteristics analysis for the motor. The motor is divided into five sub-domains according to the ventilation structure, and the fluid-thermal characteristic analysis model is established separately, as shown in Fig. 2(b). The solution domains are the end solution domain  $E_l$ , end solution domain  $E_r$ , core solution domain  $C_b$ , core solution domain  $C_r$ , and cooler solution domain. Since the cooler is symmetrically distributed along the X direction, only a 1/2 cooler model is built. In the model, a, c, h, f, j, and S2 are the mass flow inlet boundaries, and b, d, e, g, i, S1, and S3 are the pressure outlet boundaries. For the convenience of later analysis, the end windings are labeled in the direction shown by the red arrows by the numbers 1 to 180. Moreover, the number of end windings in the solution domains  $E_l$  and  $E_r$  is the same. M1 is the section of the inner air path cooler region at  $Z = 0$  mm.

The model is simplified in order to reduce the solution time. The equivalent process for the windings and insulation in the stator slot is shown in Fig. 3 [26–28]. The multiple copper conductors within the winding are combined into a single body. And a variety of insulation materials have also been merged into the equivalent insulation by multi-step equivalence, and the equivalent thermal conductivity calculation formula is expressed as follows [29].

$$k_e = k_b \frac{v_b}{v_b + v_c} + k_c \frac{v_c}{v_b + v_c} \quad (3)$$

where  $k_e$  is equivalent thermal conductivity of the insulation material (W/m·k),  $k_b$  and  $k_c$  are thermal conductivity of different insulation materials (W/m·k), respectively, and  $v_b$  and  $v_c$  are volume fraction of different insulation materials (%), respectively. Based on the layered equivalence, shell conduction is applied to simulate the heat transfer effect of the equivalent insulation and reduce the mesh number further.

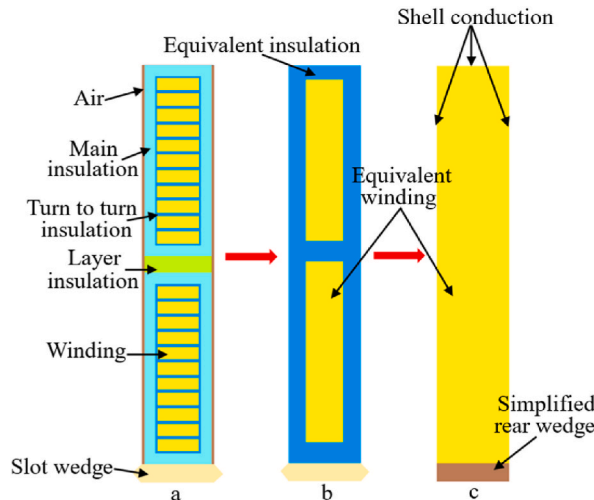


Fig. 3. Winding equivalence. (a) Actual structure of stator winding. (b) Simplified winding. (c) Equivalent winding used in this paper.

In order to accurately solve the global domain fluid-thermal characteristics of the motor, the following assumptions and boundary conditions are made:

- 1) Compared to the forced convection in the cooler and natural convection heat transfer on the housing, the amount of radiation heat transfer is minor. Therefore, the radiation heat transfer is ignored.
- 2) Ignores rotor core losses and assumes that the distribution of stator core losses is uniform.
- 3) The inlet flow rate for each solution domain is determined from the fluid field analysis results.
- 4) The ambient temperature used in the simulation is measured in experiments.
- 5) Pressure of the outlet boundary condition is 1 standard atmosphere.
- 6) The fluid-solid interface is set to the no-slip coupled wall.
- 7) The outer surface of the housing is set as the wall boundary, and the boundary conditions are:

$$\lambda \frac{\partial T}{\partial n} \Big|_{S_A} = -\alpha(T - T_f) \tag{4}$$

where  $\alpha$  is the heat dissipation coefficient [W/(m<sup>2</sup>·K)],  $T_f$  is the fluid temperature around the cooler and  $S_A$  is the cooler.

2.5. Fluid-thermal characteristic coupling analysis method

The flow chart of the global domain fluid-thermal characteristic coupling analysis method is shown in Fig. 4. At first, by solving the global domain fluid field model, the flow and pressure at the cooler inlet and outlet S1, S2, and S3 are derived. Then, assuming the cooler inlet temperature of the inner air path, the temperatures of the two cooler outlets are obtained by solving the fluid-thermal characteristic analysis model of the cooler. The temperature and flow of the two outlets are used as the inlet boundary conditions for the two end solution domains. Subsequently, the end solution domain's outlet temperature and flow are used as the inlet boundary conditions for the corresponding core solution domain. Finally, it is determined whether the average outlet temperature of the two core solution domains and the assumed cooler inlet temperature of the inner air path satisfy the convergence conditions. If not, the solution

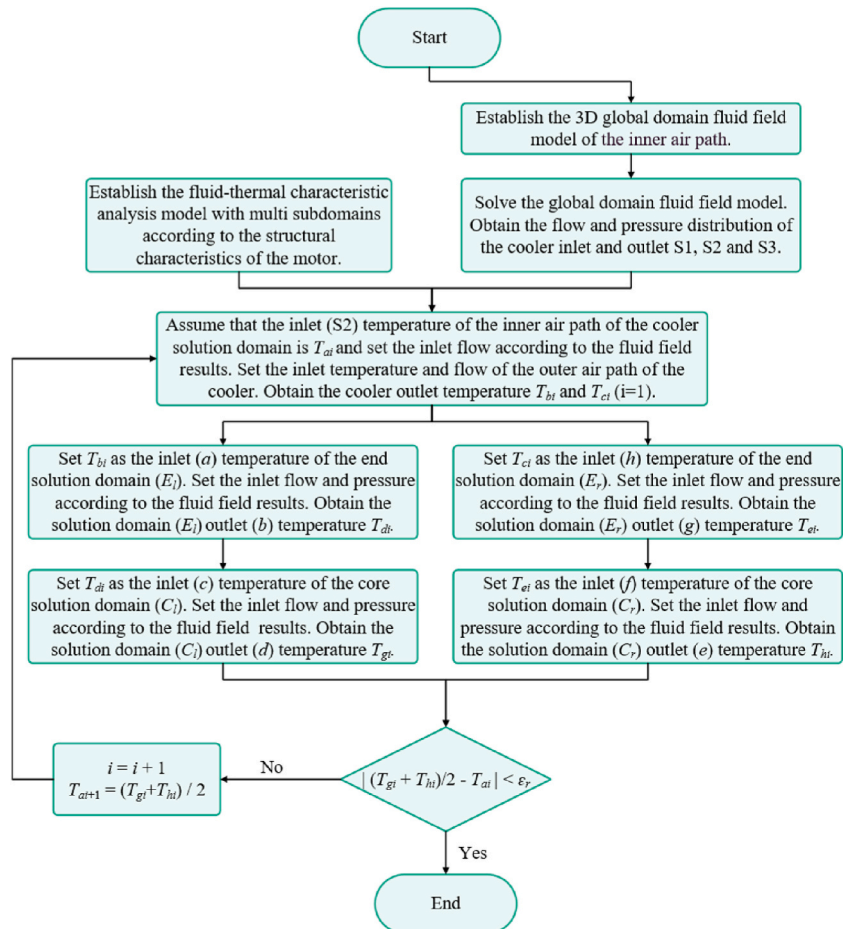


Fig. 4. Flow chart of the global domain fluid-thermal characteristic coupling analysis method.

is solved again by changing the assumed temperature until the convergence conditions are satisfied.

In addition, it needs to be particularly stated that  $E_l$  has the same fluid computational domain as  $C_l$ . The difference between the two is that  $E_l$  only contains solid structures in the end region, including the end of the stator winding, end rings, and part of the rotor bar, etc. While  $C_l$  only contains solid structures in the core region, including the stator and rotor cores, stator winding in slots, rotor bar in slots, rotor support frame, etc. And this holds applicable for  $E_r$  and  $C_r$  as well. In this way, the flow characteristics of the fluid from the cooler outlet of the inner air path are the same in  $E_l$  and  $C_l$ . When solving for the solution domain  $E_l$ , the fluid absorbs only the losses generated by the solids in the end region and warms up. Then, when solving for  $C_l$ , the warmed fluid absorbs the losses generated by the solids in the core region. This modeling approach can effectively reduce the computational cost of a single model. In addition, both the 3D global domain fluid field model and the fluid-thermal characteristic analysis model are solved by Ansys Fluent 2020 R2.

### 3. Results and discussion

#### 3.1. Global domain fluid field calculation results

The global domain fluid field model of the inner air path is solved. The streamlines of the inner air path are obtained, as shown in Fig. 5(a) and (b). As can be seen from the figures, the streamlines distribution along the inner air path is relatively uniform. The maximum fluid velocity in the inner air path is 95.6 m/s, located at the centrifugal fan blade. This is caused by the rotation of the centrifugal fan. In addition, the fluid velocity in most regions of the inner air path is within 28.7 m/s. Fig. 5(b) also shows that the fluid velocity in the air gap and the radial ventilation duct of the stator and rotor is relatively high (the red circles in Fig. 5(b)), up to 57.6 m/s. This is due to the small cross-sectional area of the flow path in this region. In addition, there are vortices at local locations in the inner air path (the black circles in Fig. 5(b)). Especially the bottom of both sides of the motor, which is mainly caused by the stator support baffle and affects the fluid flow from the end to the core region.

The fluid flow near the cooling tube is directly related to the overall heat dissipation. Fig. 5(c) shows the fluid vector distribution on the M1 section. It can be seen that the upper layer fluid velocity, which is close to the centrifugal fan, is higher than that of the lower layer fluid. The fluid velocity distribution makes the heat transfer capacity of the upper cooling tube superior to that of the lower cooling tube. Cooling tubes are arranged in a staggered manner between layers so that the direction of fluid flow is constantly changing, which helps to strengthen the heat transfer capacity of the cooling tubes. However, the vortex generated by the intersection of fluids also brings about energy loss.

In order to further study the flow pattern of the inner air path and the flow rate distribution characteristics in the stator radial ventilation duct, the outflow flow rate of each duct is shown in Fig. 5(d). It can be seen that the outflow flow rate of the stator radial ventilation duct is symmetrically distributed along the axial direction, which is characterized by being high on both sides and low in the middle. The average flow rate of the 14 ventilation ducts is 0.577 m<sup>3</sup>/s. The highest flow rate of 0.646 m<sup>3</sup>/s is found in radial ventilation duct No. 1, which is 11.96% higher than the average flow rate. Ventilation duct 6 has the lowest flow rate of 0.552 m<sup>3</sup>/s, which is 4.33% lower than the average flow rate. The dual circulation cooling structure of the inner air path makes the flow rate distribution of each radial ventilation duct relatively uniform, which helps to reduce the axial temperature difference of the motor.

The fluid velocity in the stator radial ventilation duct significantly influences the heat dissipation in the stator region. Therefore,

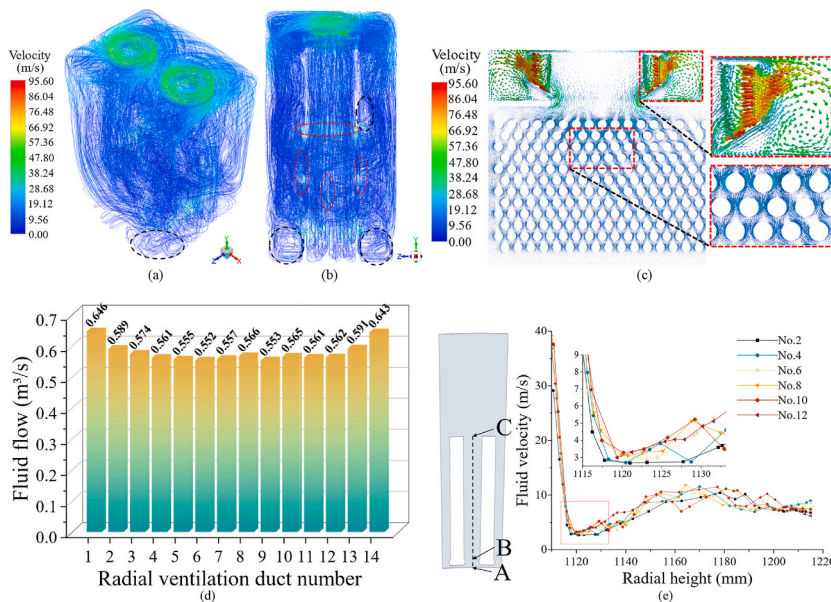


Fig. 5. Fluid characteristics. (a) Streamlines of inner air path of isometric view. (b) Streamlines of inner air path of +X view. (c) Fluid vector distribution on M1 section. (d) Flow distribution in each stator radial ventilation channel. (e) Fluid velocity variation in the stator radial ventilation duct.

the fluid velocity variation in the radial ventilation duct is analyzed using the  $X = 0$  mm section as an example. The sampling line AC is set in the 2, 4, 6, 8, 10, and 12 stator radial ventilation ducts. Point B is at 1115 mm in the positive direction along the Y-axis (radial direction).

The fluid velocity variation in the stator radial ventilation duct is shown in Fig. 5(e). It can be seen from the figure that the fluid velocity in the six radial ventilation ducts tends to decrease, increase, and then decrease along the radial direction. The velocity at the entrance of the stator radial ventilation duct reaches a maximum of 39.13 m/s in the No. 8 duct. It is because the rotor rotation drives the fluid near the air gap, increasing the flow velocity. Under the disturbance of the slot wedge, the fluid velocity decreases sharply along the radial direction. The velocity drops to a minimum of 2.69 m/s at  $Y = 1120$  mm in the No. 4 duct. In the range of  $Y = 1120-1177$  mm, the fluid velocity gradually increases, and the maximum of 11.48 m/s is located in the No. 12 duct. This is because the cooling fluid does not flow parallel into the radial ventilation duct. Therefore, there are windward and leeward sides in the ventilation duct, and the fluid velocity on the windward side is greater than that on the leeward side. Influenced by the angle of incidence, the windward side of the fluid influence is larger in the range of  $Y = 1120-1177$  mm. Therefore, the fluid velocity increases continuously. In the range of  $Y = 1177-1215$  mm, the fluid velocity turns to decrease under the influence of the fluid on the leeward side and drops to a minimum of 6.17 m/s located in the No. 12 duct. This is due to the large cross-sectional area of the ventilation duct near the stator yoke, which reduces the fluid velocity.

### 3.2. Fluid-thermal characteristic

#### 3.2.1. Motor overall temperature distribution

The temperature distribution of each sub-domain component is obtained by solving the fluid-thermal characteristic analysis model. Due to the sub-domain calculation, the average temperature of each sub-domain component is volume-weighted averaged to calculate the overall average temperature of each motor component, as listed in Table 2. It can be seen that the average temperature of the stator winding is the highest among the motor components, at 77.72 °C. Furthermore, the hot spot of the motor is also located at 120° of the circumferences of the stator end winding on the drive side, which is 89.52 °C. The lowest temperature in the motor is located in the slot wedge, at 49.14 °C. The overall temperature distribution meets class F insulation requirements.

#### 3.2.2. End solution domain temperature distribution

The end winding average temperature variations in the solution domains  $E_l$  and  $E_r$  along the circumferential direction are shown in Fig. 6. The figure shows that the end winding temperature on both ends increases and then decreases along the circumferential direction. The end winding average temperature of numbers 1 to 45 and 146 to 180 is relatively low, ranging from 71.27 °C to 76 °C. This part of the end winding is located in the upper part of the motor and is in direct contact with the cooling fluid flowing from the cooler, so the heat dissipation conditions are better. The end winding average temperature of the numbers 46 to 145 from both sides to the middle increases and reaches a maximum of 86.4 °C at the end winding of No. 118. This is due to the presence of a wind shield between the end region and the core region. The fluid in the end region flowing through the lower part of the end region is blocked by the baffle plate and forms a vortex, resulting in poor heat dissipation conditions for the end windings in this region. However, since rotor rotation affects the flow of fluid in the end region, the highest temperature is not located directly below the end, but at the end winding of No. 118.

#### 3.2.3. Core solution domain temperature distribution

The overall temperature distribution of the two core solution domains is shown in Fig. 7(a). The highest temperature in the solution domain  $C_l$  is 81.27 °C, located at the bottom of the stator winding. The highest temperature of the solution domain  $C_r$  is 79.08 °C, and its location is the same as that of the solution domain  $C_l$ . The overall temperature of the solution domain  $C_r$  is slightly lower than that of  $C_l$ . This is because the cold air in the outer air path flows from the right to the left, so the temperature of the air coming out of the cooler outlet in the inner air path is lower on the right than on the left.

The stator winding temperature distribution in the core solution domain is shown in Fig. 7(b). The maximum temperature of the stator winding in slots is 81.27 °C, and the minimum temperature is 76.45 °C. The maximum temperature difference of the stator winding in slots is 4.82 °C, which indicates that the temperature distribution of the stator winding in slots is uniform and the temperature gradient is small. Because the ventilation structure is symmetrically distributed along the axial direction, the fluid flow characteristics on both sides are similar. So, the stator winding temperature distribution characteristics on both sides are roughly the same. In addition, the average temperature of the stator winding in slots in the solution domain  $C_l$  is 2.32 °C higher than that in the solution domain  $C_r$ .

The rotor bar temperature distribution in the core solution domain is shown in Fig. 7(c). The highest temperature of the rotor bar in slots is 62.01 °C, which is located at 196° in the circumferential direction in solution domain  $C_l$  and at a distance of 297 mm from the Z

**Table 2**  
Main structure temperature of the motor.

Part	Max temperature (°C)	Min temperature (°C)	Average temperature (°C)
Stator winding	89.52	70.63	77.72
Stator core	72.25	59.00	65.59
Slot wedge	73.43	49.14	62.12
Rotor winding	84.69	57.65	65.22
Rotor core	62.01	50.81	57.47

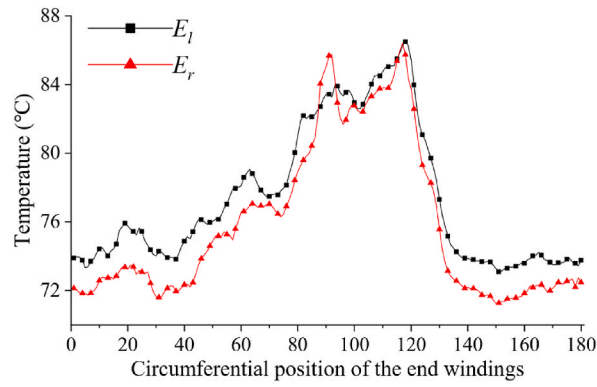


Fig. 6. Average temperature variation of the end winding.

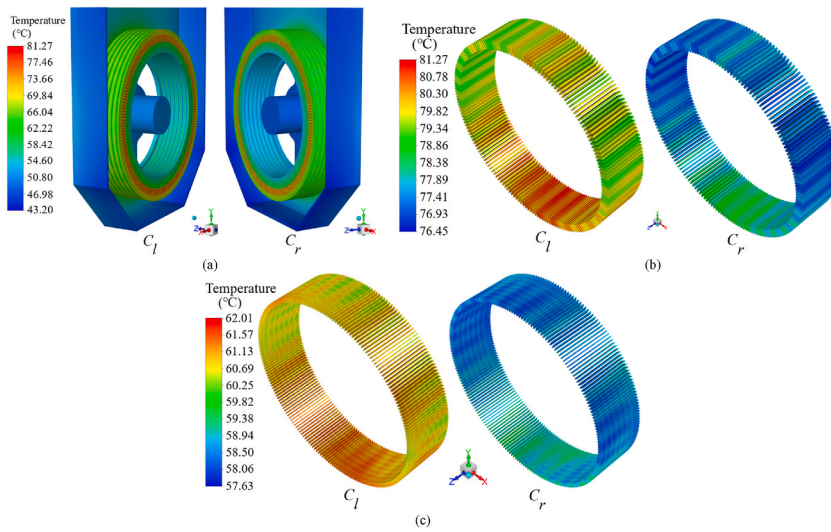


Fig. 7. Temperature distribution contour. (a) Overall temperature distribution contour of core solution domains. (b) Temperature distribution contour of the stator winding in slots. (c) Temperature distribution contour of the rotor bar in slots.

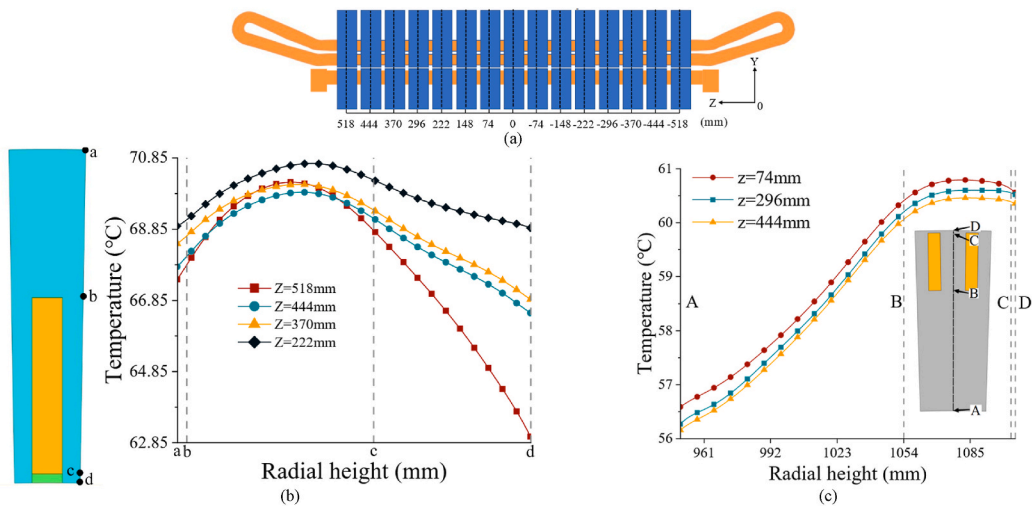


Fig. 8. Temperature variation along the radial direction. (a) Sampling lines position. (b) Stator core temperature variation along the radial direction. (c) Rotor core temperature variation along the radial direction.

= 0 mm section. The lowest temperature is 57.63 °C, located at 1° in the solution domain  $C_r$  and a distance of 30 mm from the Z = 0 mm section. Moreover, the maximum temperature difference of the rotor bar in the slots is also small, only 4.38 °C.

To further study the temperature characteristics of the stator and rotor cores along the radial and axial directions, sampling lines are selected at different axial locations. The locations of the sampling lines are displayed in Fig. 8(a).

The stator core temperature variation along the radial direction at different axial positions is shown in Fig. 8(b). The temperature increases first and then decreases along the radial direction, reaching the highest at 2/3 of the stator teeth, at 70.69 °C. This is because both sides of the stator teeth are surrounded by the stator windings. In addition to the core loss generated by the stator teeth, many copper losses are transferred to it. Therefore, the temperature reaches the highest near the center of the stator winding. Except at Z = 518 mm, the stator core temperature gradually increases along the axial direction from the end to the middle. This is because the cooling fluid flows from the end to the middle region. The closer to the axial center, the higher the fluid temperature, resulting in a lower convective heat transfer rate. As for Z = 518 mm, the sub-domain calculation sets the interface of the stator winding between the slot and the end winding as the adiabatic boundary surface, resulting in the poor axial heat dissipation condition of the winding near the interface. The temperature drop rate in the cd section of the Z = 518 mm curve is large because the stator yoke is in direct contact with the stator support structure at this location. The heat conduction rate is significantly greater than the convective heat transfer rate on the surface of the stator yoke at other axial locations.

The rotor core temperature variation along the radial direction at different axial positions is shown in Fig. 8(c). As can be seen from the figure, the temperature distribution characteristics of the rotor core are approximately the same as those of the stator core. Along the radial direction, the rotor core temperature increases first and then falls from the outer surface to the inner surface, and the high-temperature area is concentrated in the vicinity of the rotor bar. Along the axial direction, the rotor core temperature gradually

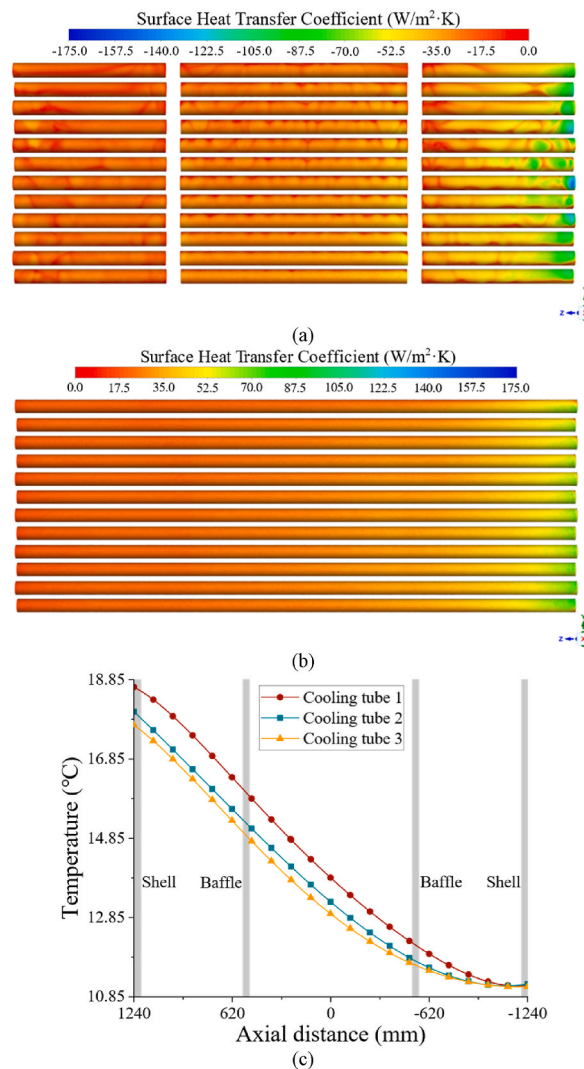


Fig. 9. Cooler solution domain. (a) Cooling tube surface heat transfer coefficient of inner air path surface. (b) Cooling tube surface heat transfer coefficient of outer air path surface.

increases from the end to the middle. Due to ignoring the rotor core loss and being far away from the heat source, the temperature gradient of the AB section is large. The BC section has a small temperature gradient along the radial direction because of its proximity to the heat source. The CD section has a decreasing temperature trend under the effect of air-gap heat exchange.

#### 3.2.4. Cooler solution domain temperature distribution

The surface heat transfer coefficient of the cooling tube is shown in Fig. 9(a) and (b). It can be seen that the convective heat transfer coefficient on the right side is significantly greater than that on the left side, both in the inner air path and the outer air path. This is because the cold air in the outer air path flows from right to left. The low temperature fluid gradually increases in temperature along the flow path. The temperature difference between the two sides of the cooling tube at the outlet side is lower than that at the inlet side, resulting in a lower surface heat transfer coefficient.

In addition, comparing Fig. 9(a) and (b), it can be found that the inner air path surface heat transfer coefficient distributes unevenly, while that of the outer air path is with a small gradient and is evenly distributed. This is because the fluid velocity near the inner air path cooling tube surface is not uniformly distributed due to the cooling tube arrangement. The fluid velocity near the outer air path surface is affected by the boundary layer, so the velocity variation along the axial direction is small.

The outer air path fluid temperature variation along the axial direction at the cooling tube axial section center is shown in Fig. 9(c) (the cooling tube number is shown in Fig. 2(b)). It can be seen that the fluid temperature gradually increases from the inlet side to the outlet side. The fluid temperature in the upper layer of the cooling tube is higher than in the lower layer. The temperature rise of the fluid in cooling tube No. 1 is the highest, at 7.56 K, and the lowest in tube No. 3, at 6.61 K. This is because the upper cooling tube is close to the centrifugal fan. Therefore, the fluid velocity near the upper cooling tube is higher than that of the lower, resulting in a higher heat transfer rate.

## 4. Experimental verification

An experimental platform is built in order to verify the rationality of the developed model and the effectiveness of the proposed method. The experimental platform includes a prototype, a thermo-sensitive wind speed measuring instrument, a resistance measuring instrument, and a console, as shown in Fig. 10.

Firstly, air speed and temperature measurement tests are conducted. Eight measuring holes are reserved on both sides of the cooler, and the positions of the measuring holes correspond to the inlet and outlet of the cooler. Multiple measurements at different depths for each measurement point are performed to obtain the average air speed and temperature. Then, the thermal test is conducted following the national standard GB/T1032. The resistance of the stator winding at the beginning and end of the thermal test is measured to calculate the average temperature of the stator winding. In addition, the ambient temperature at the time of the experiment is measured, which is 11.1 °C.

The calculated results and measured values are listed in Table 3. As seen from the table, the relative error between the calculated and measured values of the average temperature of the winding is only 0.57%, and the maximum error of the fluid field results is 4.92%. This is because of the uneven distribution of the inlet and outlet fluid velocities in the inner air path of the cooler. The experiment can only measure the fluid velocity at one point. It cannot obtain the average fluid velocity of the inlet and outlet surfaces, so the relative error is large. The air speed, temperature, and motor thermal tests meet the engineering calculation requirements. It shows that the numerical simulation results are consistent with the actual situation, which verifies the rationality of the developed model and the effectiveness of the proposed method.

## 5. Conclusion

This paper investigated a 6.5 MW positive-pressure explosion-proof air-air cooled induction motor. A global domain fluid field model and a partitioned fluid-thermal characteristic coupling analysis model were established and solved, respectively. The following conclusions were obtained:

- (1) The sub-domain fluid-thermal characteristics analysis models were coupled and solved using global domain fluid field results. The global fluid flow and temperature characteristics were obtained. The maximum relative error between the numerical calculations and measured values was 4.92%. It proved that the developed model and method are effective and accurate in studying motors with large capacities and complex ventilation structures.
- (2) The fluid distribution in the motor was reasonable, and the fluid traces were relatively evenly distributed. The maximum difference in flow between different stator radial ventilation ducts reaches 16.2%. The air gap contributed 6.7% of the stator core flow. The maximum fluid velocity in the inner air path was 95.6 m/s, located at the outer edge of the centrifugal fan. The fluid velocity increased as it approached the centrifugal fan and decreased as it moved away. The lowest was at the bottom of the end region.
- (3) The overall temperature distribution of the motor was low at both ends and high in the middle. The hotspot temperature was 89.52 °C, located at 120° in the circumferential direction of the end winding within the end solution domain  $E_l$ . The average temperature of the stator winding in the solution domain  $C_l$  was 2.25 °C higher than that in the solution domain  $C_r$  due to fluid flow direction in the outer air path. In addition, the temperature of the lower half of the motor was higher than that of the upper half. This was due to the poor fluid condition in the lower half, resulting in lower heat dissipation efficiency.



Fig. 10. Prototype experimental platform.

Table 3

Calculated results and measured values.

	Calculated result	Measured value	Relative error
Inlet velocity of the inner air path (m/s)	8.69	9.14	4.92%
Outlet velocity of the inner air path (m/s)	7.65	7.92	3.41%
Outlet temperature of the outer air path (°C)	23.83	23.9	1.67%
Average temperature of the stator winding (°C)	77.72	78.1	0.57%

#### Author statement

Yongming Xu: Funding acquisition, Conceptualization, Methodology, Supervision.

Ziyi Xu: Formal analysis, Investigation, Writing - Original Draft, Writing - Review & Editing, Qianwen Zhao: Validation, Resources, Visualization.

Yaodong Wang: Software, Data Curation.

#### Declaration of competing interest

The authors declare that they have no known competing financial interests or personal relationships that could have appeared to influence the work reported in this paper.

#### Data availability

The authors do not have permission to share data.

#### Acknowledgments

This work was supported in part by the National Natural Science Foundation of China, under Grants (52077047), and in part by Changzhou Science and Technology Bureau, under Grants (CZ20220023).

#### References

- [1] M. D'Souza, I. Malek, T. Rahill, API 541 variable speed medium voltage motors applied in a class I, division 1 hazardous location—a case study, *IEEE Trans. Ind. Appl.* 53 (1) (Jan.-Feb. 2017) 731–738.
- [2] X. Wang, B. Li, D. Gerada, K. Huang, I. Stone, S. Worrall, Y. Yan, A critical review on thermal management technologies for motors in electric cars, *Appl. Therm. Eng.* 201 (2022), 117758.
- [3] A. Zarghani, H. Torkaman, N. Arbab, M. Sedigh Toulabi, Lumped parameter thermal network for thermal analysis of a rotor-excited axial flux switching machine with electromagnetic-thermal design, *Measurement* 193 (Apr. 2022), 110971.

- [4] M. Cavazzuti, G. Gaspari, S. Pasquale, E. Stalio, Thermal management of a Formula E electric motor: analysis and optimization, *Appl. Therm. Eng.* 157 (Jul. 2019), 113733.
- [5] M. Stebel, et al., Thermal analysis of 8.5 MVA disk-type power transformer cooled by biodegradable ester oil working in ONAN mode by using advanced EMAG-CFD-CFD coupling, *Int. J. Electr. Power Energy Syst.* 136 (Mar. 2022), 107737.
- [6] A. Tiwari, S. Yavuzkurt, Iterative conjugate heat transfer analysis for heat transfer enhancement of an externally cooled three-phase induction motor, *IET Electr. Power Appl.* 11 (1) (Jan. 2017) 99–107.
- [7] D.-D. Dang, X.-T. Pham, P. Labbe, F. Torriano, J.-F. Morissette, C. Hudon, CFD analysis of turbulent convective heat transfer in a hydro-generator rotor-stator system, *Appl. Therm. Eng.* 130 (Feb. 2018) 17–28.
- [8] S. Nategh, H. Zhang, O. Wallmark, A. Boglietti, T. Nassen, M. Bazant, Transient thermal modeling and analysis of railway traction motors, *IEEE Trans. Ind. Electron.* 66 (1) (Jan. 2019) 79–89.
- [9] A. Acquaviva, O. Wallmark, E.A. Grunditz, S.T. Lundmark, T. Thiringer, Computationally efficient modeling of electrical machines with cooling jacket, *IEEE Trans. Transport. Electrific.* 5 (3) (Sep. 2019) 618–629.
- [10] S.-C. Sung, S.-K. Kim, M.-D. Oh, Numerical analysis of the cooling performance of a totally enclosed air-to-air cooled motor using a dual cell heat exchanger model, *J. Mech. Sci. Technol.* 35 (6) (Jun. 2021) 2719–2731.
- [11] M.L. Hosain, R. Bel Fdhila, K. Rönnerberg, Taylor-Couette flow and transient heat transfer inside the annulus air-gap of rotating electrical machines, *Appl. Energy* 207 (Dec. 2017) 624–633.
- [12] C. Kim, K.-S. Lee, Numerical investigation of the air-gap flow heating phenomena in large-capacity induction motors, *Int. J. Heat Mass Tran.* 110 (Jul. 2017) 746–752.
- [13] A. Tikadar, D. Johnston, N. Kumar, Y. Joshi, S. Kumar, Comparison of electro-thermal performance of advanced cooling techniques for electric vehicle motors, *Appl. Therm. Eng.* 183 (Jan. 2021), 116182.
- [14] K. Bersch, S. Nuzzo, P.H. Connor, C.N. Eastwick, R. Rolston, M. Galea, Thermal and electromagnetic stator vent design optimisation for synchronous generators, *IEEE Trans. Energy Convers.* 36 (1) (Mar. 2021) 207–217.
- [15] M. Appadurai, E. Fantin Irudaya Raj, K. Venkadeshwaran, Finite element design and thermal analysis of an induction motor used for a hydraulic pumping system, *Mater. Today Proc.* 45 (Mar. 2021) 7100–7106.
- [16] H. Sasa, et al., Electromagnetic-thermal coupled analysis considering AC losses in REBCO windings of 10 MW fully superconducting synchronous generators cooled by subcooled liquid nitrogen for electric aircraft, *IEEE Trans. Appl. Supercond.* 32 (6) (Sept. 2022) 1–6.
- [17] J.H. Kim, et al., Design and analysis of cooling structure on advanced air-core stator for megawatt-class HTS synchronous motor, *IEEE Trans. Appl. Supercond.* 27 (4) (Jun. 2017) 1–7.
- [18] C. Carounagarane, T.R. Chelliah, D. Khare, Analysis on thermal behavior of large hydrogenerators operating with continuous overloads, *IEEE Trans. Ind. Appl.* 56 (2) (Mar. 2020) 1293–1305.
- [19] C. Cotas, et al., Numerical study of transient flow dynamics in a core-type transformer windings, *Elec. Power Syst. Res.* 187 (Oct. 2020), 106423.
- [20] Y.J. Kim, M. Jeong, Y.G. Park, M.Y. Ha, A numerical study of the effect of a hybrid cooling system on the cooling performance of a large power transformer, *Appl. Therm. Eng.* 136 (May 2018) 275–286.
- [21] G.R. Rodriguez, L. Garelli, M. Storti, D. Granata, M. Amadei, M. Rossetti, Numerical and experimental thermo-fluid dynamic analysis of a power transformer working in ONAN mode, *Appl. Therm. Eng.* 112 (Feb. 2017) 1271–1280.
- [22] E. Galloni, P. Parisi, F. Marignetti, G. Volpe, CFD analyses of a radial fan for electric motor cooling, *Therm. Sci. Eng. Prog.* 8 (Dec. 2018) 470–476.
- [23] S. Hyeon, C. Kim, K. Lee, Thermal enhancement of an air-cooled motor with a flow guide, *Int. J. Heat Mass Tran.* 183 (Feb. 2022), 122228. Part C).
- [24] I. Haq, et al., Characteristics of chemical processes and heat source/sink with wedge geometry, *Case Stud. Therm. Eng.* 14 (2019), 100432.
- [25] Ansys Fluent 2020R2 Theory Guide, ANSYS, Inc., Canonsburg, PA, 2020.
- [26] A. Boglietti, E. Carpaneto, M. Cossale, S. Vaschetto, M. Popescu, D.A. Staton, Stator winding thermal conductivity evaluation: an industrial production assessment, *IEEE Trans. Ind. Appl.* 52 (5) (Sep. 2016) 3893–3900.
- [27] S. Horrigue, I.A. Abbas, Fractional-order thermoelastic wave assessment in a two-dimensional fiber-reinforced anisotropic, *Material*, *Mathematics* 8 (9) (Sep. 2020), 1609.
- [28] T. Saeed, I.A. Abbas, The effect of fractional time derivative on two-dimension porous materials due to pulse heat flux, *Mathematics* 9 (3) (Jan. 2021) 207.
- [29] N. Simpson, R. Wrobel, P.H. Mellor, Estimation of equivalent thermal parameters of impregnated electrical windings, *IEEE Trans. Ind. Appl.* 49 (6) (Nov./Dec. 2013) 2505–2515.